JOURNAL OF APPLIED CRYSTALLOGRAPHY
ISSN 1600-5767

The linear phase correction of modulation of intensity emerging from zero effort (MIEZE) with magnetic Wollaston prisms

Fankang Li*

Neutron Technologies Division, Oak Ridge National Laboratory, Oak Ridge, TN 37830, USA. *Correspondence e-mail: frankli@ornl.gov

Received 17 May 2021
Accepted 10 December 2021

Edited by G. J. McIntyre, Australian Nuclear Science and Technology Organisation, Lucas Heights, Australia

Keywords: modulation of intensity emerging from zero effort; MIEZE; linear phase correction; magnetic Wollaston prisms; neutron spin echo.

This study proposes the use of two magnetic Wollaston prisms (MWPs) to correct for the linear Larmor phase aberration of modulation of intensity emerging from zero effort (MIEZE), introduced by the transverse size of the sample. With this approach, the contrast of the intensity modulation can be maximized at any scattering angle of interest such that the same contrast as the direct transmission geometry can be fully recovered. The optimum magnetic fields required for the MWPs depend only on the scattering angle and the frequencies of the radio-frequency flippers, and they are independent of the neutron wavelength and beam divergence, which makes the approach suitable for both pulsed and continuous neutron sources.

1. MIEZE and its Larmor phase aberration

The dynamical properties of materials are often the key to understanding their macroscopic properties. A technique that can reach the time scales with a matching length scale is greatly desired to investigate the dynamics in soft matter materials such as proteins (Rheinstädter *et al.*, 2006), polymers (Godfrin *et al.*, 2015) and hard condensed matter materials such as superconductors (Blackburn *et al.*, 2006; Haslbeck *et al.*, 2019; Keller *et al.*, 2006). The neutron spin echo (NSE) technique satisfies this demand by employing the Larmor labeling of neutron spins in a magnetic field, which decouples the energy resolution of a neutron instrument from the width of the wavelength band and thus provides us with another approach to achieve ultra-high resolution (Mezei, 1972). To implement NSE, two static magnetic fields are required with one on each side of the sample. The neutron spin will precess continuously inside the two magnetic fields through the sample region, where the neutron spin is flipped and the Larmor phase accumulation will be reversed. Any energy exchange between the neutron and the sample can be encoded as a change in the accumulated neutron Larmor phase. However, certain situations, such as samples that would depolarize the neutron beam or require high magnetic field, would be challenging for NSE. Even though paramagnetic (Murani & Mezei, 1980), ferromagnetic (Mezei *et al.*, 2003) and intensity-modulated NSE (Farago & Mezei, 1986) techniques have been developed, either they cannot be applied due to the depolarizing sample environment or they are too complicated to be routinely operated. All of these difficulties prohibit conventional NSE from accessing the full arena of magnetic phenomena, for example, the spin dynamics in ferromagnetic superconductors (Haslbeck *et al.*, 2019), the spin-wave fluctuations in ferromagnets (Säubert *et al.*, 2019)

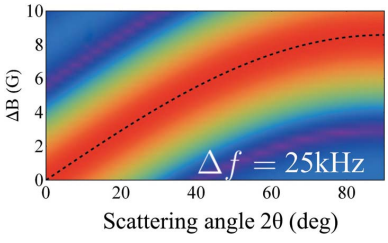

and the paramagnetic-to-skyrmion lattice transition in transition metal helimagnets (Kindervater *et al.*, 2019).

An alternative approach to allow for the complicated sample environment that involves high magnetic field and depolarizing sample is to use modulation of intensity emerging from zero effort (MIEZE) (Gähler *et al.*, 1992), which has been demonstrated or routinely operated at several neutron facilities, including Larmor at ISIS (Geerits *et al.*, 2019), ORNL (Brandl *et al.*, 2012; Dadisman *et al.*, 2020; Zhao *et al.*, 2015), CMRR (Liu *et al.*, 2020), RESEDA of FRM-II (Franz *et al.*, 2019) and VIN ROSE at J-PARC (Hino *et al.*, 2013). Depending on the direction of the static magnetic field inside the radio-frequency (RF) flippers with respect to the beam, there are longitudinal and transverse configurations for MIEZE. MIEZE requires two neutron resonance RF spin flippers before the sample and they are operated at different RF frequencies ($\omega_{1,2} = 2\pi f_{1,2}$), as shown in Fig. 1. With such spin flippers, the polarization vector of the neutron beam, which is the average direction of the neutron spin, can be modulated sinusoidally, with the phase determined by the phase angle of the RF signal (Hank *et al.*, 1997). After the beam has passed through the neutron polarization analyzer, which only transmits the polarization vector along one direction, the polarization modulation can be converted into intensity modulation before the beam interacts with the sample, as shown in Fig. 1(*a*). The intensity modulation takes the form $I(t) = A\cos[2(\omega_2 - \omega_1)t] + I_0$. Because no spin manipulation or analysis is performed afterwards, the neutron beam is no longer sensitive to the factors that can depolarize it in the sample or sample environment, which allows MIEZE to be used for complicated magnetic sample environments or depolarizing samples. When scattered by the sample quasi-elastically or inelastically, the neutrons' energy may be slightly changed, which can cause a time advance or delay in their arrival at the detector. Therefore, the contrast of the modulation (A/I_0) will be changed, from which the intermediate scattering function of the sample can be deduced (Gähler *et al.*, 1992; Golub *et al.*, 1994).

However, one of the problems of MIEZE is the variation of neutron time of flight (TOF) from the position of scattering at the sample to the position of capture at the detector. This can directly introduce a Larmor phase variation and hence phase aberration on the detector, especially for large scattering angles. To resolve this problem, the contribution of both the sample and detector geometry to the neutron TOF needs to be investigated. For the detector side, there have been extensive discussions about using post data reduction to reconstruct the contrast of the intensity modulations (Schober *et al.*, 2019; Oda *et al.*, 2020) by shifting the modulation on each pixel of the detector with a known phase. However, the application of such a reduction method is still limited, especially for a sample with large transverse size, as it cannot differentiate the locations where the neutrons are scattered at the sample position. For the sample side, as stated by Brandl *et al.* (2011) and Weber *et al.* (2013), rotating the sample with respect to the beam can also change the resolution function of the MIEZE because it changes the neutron TOF from the sample to the detector. However, rotating a flat sample is only practical within limits and it will also significantly restrict the choices of sample. It has also been suggested by Martin (2018) that the

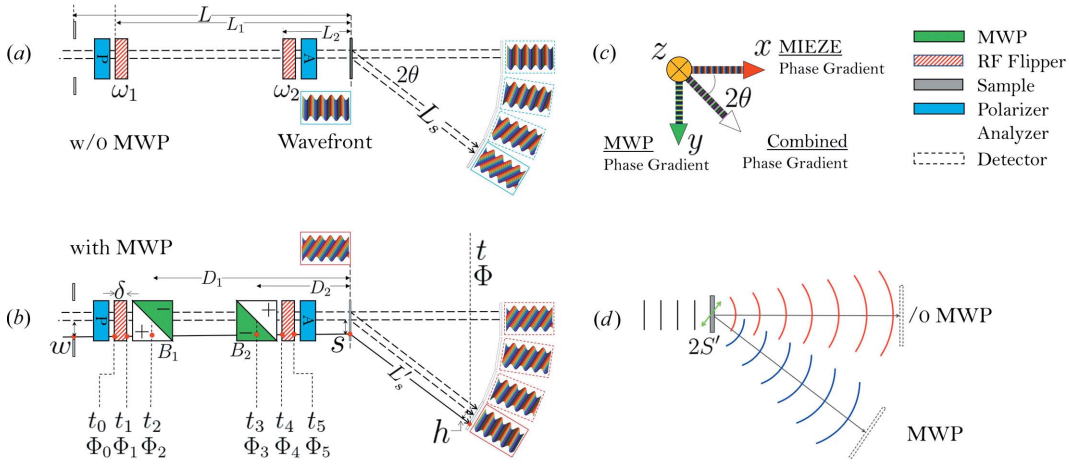

Figure 1
(*a*) The conventional transverse MIEZE setup. (*b*) The MIEZE setup combined with magnetic Wollaston prisms (MWPs) to correct for the linear Larmor phase from the sample. (*c*) A schematic of the combined intensity modulation in the time and space domains. (*d*) The intensity modulation in direct transmission and scattering directions. The lines denote the wavefront, and $2S'$ is the footprint of the sample projected towards the scattering direction, which denotes the effective source size of the intensity modulation. The frequencies of the RF flippers are $\omega_{1,2} = 2\pi f_{1,2}$ and the thickness of the RF flipper is δ. The magnetic fields inside the MWPs are $B_{1,2}$, respectively. $L_{1,2}$ and $D_{1,2}$ are the distances from the RF flippers and MWPs to the sample, respectively. The intensity modulation of the neutron beam is developed from the RF flippers in the time domain and a snapshot of the modulation is shown at the sample and detector position for a parallel beam, for the case of without (*a*) and with (*b*) the MWPs. *s* and *h* are the positions where the neutrons are scattered and captured at the sample and detector, respectively, which have a full width of $2S$ and $2H$, respectively. *w* is the transverse offset of the neutron's trajectory at the entrance of the slit located at $x = L$ with a full size of $2W$. For demonstration purposes, the dashed trajectories are the ideal case where both the incoming and outgoing neutron beams are parallel to the center trajectory. The solid trajectory shows the actual case in the experiment, which is used in the following calculations. The red dots along the neutron trajectory are the intersection points with various components of the setup, and the corresponding Larmor phase and time at these points are denoted as Φ_i and t_i, respectively.

detector can be simply configured to be parallel to the sample surface such that the neutron TOF from the sample to the detector is equal for all the neutron trajectories. However, this approach provides a complete correction only in the ideal case when the scattered neutron trajectories are parallel to the center line shown in Fig. 1(*a*), and there is a one-to-one correspondence between the scattering location at the sample and the pixel of the capture on the detector. In reality, the neutrons scattered by a specific location of the sample can be captured by any pixel of the detector and vice versa. The effectiveness of having the detector parallel to the sample surface has also been investigated with *McStas* simulations (Dadisman *et al.*, 2022); this shows that, to minimize the Larmor phase aberration, the detector needs to be perpendicular to the scattered neutrons instead of the incoming beam. Another approach is to physically rotate the RF flippers (Dadisman *et al.*, 2022) such that the wavefront of the intensity modulation can be shaped spatially to match the scattering angle without changing the neutron TOF from the sample to the detector, but its performance is sensitive to the beam divergence because the space focusing condition is coupled with the time focusing condition and they cannot be independently tuned to be focused towards different planes.

In this report, I propose to use two magnetic Wollaston prisms (MWPs) in addition to the conventional MIEZE setup such that we can precisely manipulate the Larmor phase of the neutron beam spatially to match the scattering angle of interest. Therefore, the resolution function of MIEZE can be maximized at any scattering angle of interest without any physical rotation of the sample or the RF flippers. In the following demonstration, for simplicity, both the incoming and scattered neutrons are parallel to the beam center line with no wavelength dispersion. The neutron intensity modulation will be taken as waves, which originate from the RF flippers, are scattered by the sample and propagate towards the detector, similar to ripples in water. As shown in Fig. 1(*a*), the wavefront of the incident modulation is perpendicular to the beam direction at the sample position, as well as the detector position in the direct transmission geometry. However for the detector at an angle (2θ), the arrival time of a neutron will vary depending on the position of the scattering event at the sample position (s). The consequent wavefront of the scattered neutrons will be tilted and misaligned with the detector plane. As discussed previously, for a realistic beam, the pixelated intensity modulations could only be partially corrected by post data reduction. Without knowing where the neutrons are scattered from the sample, the TOF variation and hence phase variation caused by the transverse size of the sample cannot be corrected. Also, the phase variation will change with scattering angle, which means that the resolution of MIEZE, especially at large scattering angles, will be greatly limited. Without resolving this problem, it would be challenging to further increase the energy resolution, especially at large scattering angles, unless one could compromise the size of the sample and thus neutron intensity.

MIEZE, with two RF flippers operated at different frequencies $\omega_{1,2}$, generates a Larmor phase gradient in the time domain along the **x** direction, as shown in Fig. 1(*c*). With this phase gradient in the time domain, the neutron spin can pick up a Larmor phase as it moves forward. By the time it is captured at the detector position, the Larmor phase it accumulates is $\Phi(t) = 2\Delta\omega t = 2(\omega_2 - \omega_1)t$, where t is the clock time of the detector. When a neutron travels in a magnetic field, its spin will pick up a Larmor phase that is proportional to the neutron wavelength and the magnetic field integral along the neutron trajectory. For an MWP constructed using two oppositely directed, triangular cross section magnetic fields separated by a planar interface, a gradient in the magnetic field integral can be generated when neutrons are transmitting through (Li *et al.*, 2014). Therefore, a linear Larmor phase gradient and hence modulation along the transverse direction (**y**) will be generated, as shown in Fig. 1(*c*). If both the RF flippers and the MWPs were employed, the neutron spin would experience a Larmor phase gradient in both the time domain (along the **x** direction) and the space domain (along the **y** direction) simultaneously, which is not the case in conventional MIEZE. Therefore, with the addition of the MWPs, the gradient direction of the total Larmor phase can be changed from the **x** direction to any direction in the xy plane by choosing the right combination of the phase gradients in the two directions (**x** and **y**), as shown in Figs. 1(*b*), 1(*c*) and 1(*d*). Since the direction of the phase gradient determines the wavefront of the intensity modulation, it can be adjusted such that the wavefront is always perpendicular to the average neutron trajectory and thus parallel to the detector plane. The phase aberrations can thus be minimized.

2. Larmor phase of MIEZE with magnetic Wollaston prisms

Before showing the total Larmor phase a neutron picks up through the setup in Fig. 1(*b*), I will briefly discuss the Larmor phase contributed by an individual RF flipper and MWP. As given by Golub & Gähler (1987), the Larmor phase generated by a neutron RF flipper with an angular frequency of ω is given by $\Phi_f = 2\Phi_{\rm rf}(t_i) + \omega t_\pi - \phi_i$. $\Phi_{\rm rf} = \omega t_i$ is the phase of the RF flipper upon the entrance of the neutron at t_i. t_π is the time the neutron stays inside the flipper, and it is given by $t_\pi = \delta/(v\cos\psi)$ with ψ being the divergence angle, δ the thickness of the flipper and v the neutron speed. ϕ_i is the phase the neutron spin carries before entering the RF flipper. For a MWP, as given by Li *et al.* (2014, 2016) and Li & Pynn (2014), the Larmor phase generated (Φ_m) depends on the magnetic field integral along the neutron's trajectory $\Phi_m(B, y, \psi) = (2\gamma/v)By[\cot\beta + (\cot\beta)^2\psi]$, where γ is the neutron gyromagnetic ratio, B is the magnitude of the magnetic field of the MWP, β is the inclination angle of the hypotenuse of the MWP with respect to the beam and y is the transverse coordinate of the intersection point of the beam with the midplane of the MWP, as denoted by the red dots in Fig. 1(*b*). With Φ_m, the MWP can be taken as a device with no thickness along the beam. With each neutron's transverse coordinates, divergence and velocity known, the Larmor phase picked up inside the MWP can be calculated. In the following calculations, the

Table 1
The propagation of the Larmor phase in the proposed MIEZE setup.

Φ_i and t_i are, respectively, the Larmor phase of neutron spin and time at the intersection points of the neutron trajectory and the spin manipulation components. Fig. 1 provides detailed definitions of the parameters.

Position	Time (t_i)	Neutron phase (Φ_i)
Entrance of RF_1	t_0	$\Phi_0 = 0$
Exit of RF_1	t_1	$\Phi_1 = 2\omega_1\left(t_0 + \dfrac{\delta}{2v\cos\psi}\right) - \Phi_0$
Center of MWP_1	t_2	$\Phi_2 = \Phi_m(B_1, y_1, \psi) + \Phi_1$
Center of MWP_2	t_3	$\Phi_3 = \Phi_m(B_2, y_2, \psi) + \Phi_2$
Entrance of RF_2	t_4	$\Phi_4 = \Phi_3$
Exit of RF_2	t_5	$\Phi_5 = 2\omega_2\left(t_4 + \dfrac{\delta}{2v\cos\psi}\right) - \Phi_4$
Detector	t	$\Phi = \Phi_5$

$t_0 = t - (1/v)[L_1(1+\psi^2)^{1/2} + L_s']$. $y_1 \simeq -D_1\psi - s$. $y_2 \simeq -D_2\psi - s$. $t_4 = t - (1/v) \times [L_2(1+\psi^2)^{1/2} + L_s']$. $L_s' = [h^2 + L_s^2 + s^2 - 2s(h\cos 2\theta + L_s \sin 2\theta)]^{1/2}$.

inclination angle of the MWP is assumed to be 45°. For a neutron trajectory incident upon the sample with an offset of s and divergence of ψ as indicated by the solid black line in Fig. 1(*b*), the intersection points with each device are denoted by the red dots. The coordinates of the intersection in time and space and the corresponding Larmor phase have been calculated and are shown in Table 1; using these values the Larmor phase Φ_i can be calculated at each point. By propagating the Larmor phase through all the components in Fig. 1, the phase $\Phi(t)$ at the detector can be obtained, which is given in equation (1):

$$\begin{aligned}\Phi(t) = {} & \underbrace{2(\omega_2 - \omega_1)t}_{1} + \frac{1}{v}\Bigg(\underbrace{2(\omega_1 L_1 - \omega_2 L_2)(1+\psi^2)^{1/2}}_{2} \\ & + (\omega_1 - \omega_2)\Big\{-\delta\sec\psi \\ & + 2[\underbrace{L_s^2}_{2} + \underbrace{h^2 + s^2 - 2s(h\cos 2\theta + L_s\sin 2\theta)}_{3}]^{1/2}\Big\} \\ & + 2\gamma\Big[\underbrace{(B_1 - B_2)s}_{4} + \underbrace{(B_1 D_1 - B_2 D_2)\psi}_{5}\Big](1+\psi)\Bigg) \\ \simeq {} & 2(\omega_2 - \omega_1)t + \frac{2}{v}\Big\{\underline{\omega_1(L_1 + L_s) - \omega_2(L_2 + L_s)} \\ & + \underline{\gamma\psi(B_1 D_1 - B_2 D_2)} \\ & + s\Big[\underline{\gamma(B_1 - B_2) - (\omega_1 - \omega_2)\sin 2\theta}\Big]\Big\}. \end{aligned} \tag{1}$$

In this equation, B_i denotes the magnitude of the magnetic field inside the two MWPs. L_i, D_i and L_s are the distances from the centers of the RF flippers, MWPs and detector to the sample, respectively. w, s and h are the transverse displacement of the neutron trajectory at the slit, sample and detector, respectively. In the calculation, the divergence angle can be explicitly defined as $\psi \simeq (w - s)/L$, where L is the distance from the slit to the sample position. The terms labeled with different numbers in equation (1) represent the major terms that contribute to the Larmor phase, whereas the terms that are not labeled are higher-order terms and thus are negligible. The term labeled as 1 denotes the intensity modulation produced by the RF flippers. The Larmor phase aberration, due to the dispersion of neutron speed (v), the transverse offset of scattering (s) and the distribution of scattering angles (2θ), is explicitly given as 2 and 3. The Larmor phase generated by the MWP is provided by 4 and 5, which are time independent. Term 1 is the main MIEZE signal of interest. Terms 2 and 3 are the aberration terms contributed from the sample size, scattering angle, neutron speed *etc*., which need to be minimized by the correction. In a MIEZE setup, the sample size (∼2 cm) and the area of interest on the detector (∼10 × 10 cm) are considerably smaller than the length of the scattering arm (L_s > 2 m), and also the divergence of the incident beam is small. Therefore, equation (1) can be further expanded in s, h and ψ. With the lowest orders summarized in equation (1), for the speed-dependent terms, I will minimize their contributions by setting each of the underlined combinations to zero, yielding the following:

$$\text{Time focusing: } \omega_1(L_1 + L_s) = \omega_2(L_2 + L_s), \tag{2}$$

$$\text{Space focusing: } B_1 D_1 = B_2 D_2, \tag{3}$$

$$\text{Steering condition: } B_2 - B_1 = \frac{1}{\gamma}(\omega_2 - \omega_1)\sin 2\theta. \tag{4}$$

Equation (2) is termed the time focusing condition or the MIEZE condition. In a conventional MIEZE setup without MWPs, it can remove the speed dependence of the Larmor phase for the directly transmitted neutron beam. Equation (3) can ensure the Larmor phase the neutron spin accumulates through the MWPs is independent of the beam divergence. With such a condition, the wavefront of neutron spin can be tilted with respect to the incident beam direction by the same amount regardless of the divergence angle (ψ). For a given scattering angle (2θ) and RF frequency ($\omega_{1,2}$), to ensure the wavefront can be tilted by the right amount, equation (4) needs to be satisfied. Similar to the phased array radar, equation (4) can ensure the scattered beam is modulated with high contrast towards the detector at a specific angle; I call it the steering condition. Equations (3) and (4) combined yield the optimum field required for the MWPs to correct for the linear phase aberrations caused by the transverse dimension of the sample in a regular MIEZE. In combination with equation (2), the Larmor phase of neutron spin at the detector position would be independent of the neutron speed and beam divergence to the first order, which is the prerequisite condition to maximize the contrast of the MIEZE signal.

To understand the principle of this method more intuitively, note that the introduction of the two MWPs can generate a magnetic field integral gradient along the transverse direction (**y**) as shown in Fig. 1(*c*), which is perpendicular to the Larmor phase gradient direction generated by the RF flippers (**x**). With the two independent phase gradients, the combined gradient direction of the total Larmor phase can be steered to any direction of interest. Since the phase gradient direction is

always perpendicular to the wavefront of the intensity modulation, it can be tuned such that it is perpendicular to the surface of the detector. In this case, the wavefront will be parallel to the detector and the phase aberrations can be minimized. Additionally, when the scattering angle is small ($2\theta \simeq 0$), no field is required for the MWPs ($B_{1,2} = 0$). As also shown by equation (4), the field required for the MWPs is independent of neutron wavelength, which makes the setup capable of accepting a broad wavelength band at both pulsed and continuous neutron sources.

The employment of MWPs to steer the wavefront of the intensity-modulated neutron beam is very similar to a phased array radar, which can create a beam of radio waves that can be electronically steered to point in different directions without moving the antennas. With such analogy, the approach of rotating the RF flippers is similar to the conventional radar, which rotates physically and steadily to sweep the airspace with a narrow beam (Dadisman *et al.*, 2022). As illustrated in Fig. 1(*d*), as the scattering angle increases, the footprint of the sample or the effective sample size ($2S' = 2S\cos 2\theta$) will decrease. Hence as the scattering angle is approaching $2\theta = 90^\circ$, the intensity modulations get more 'coherent', which means fewer aberrations will be contributed from the transverse size of the sample. Ultimately, with $2\theta = 90^\circ$, the sample becomes a coherent point source of intensity modulations. These effects will be shown and discussed in the following sections.

3. The phase correction calculations of MIEZE

With the Larmor phase known in equation (1), the time modulations measured by the detector can be calculated by integrating over the beam size (w) and sample size (s) and thus divergence ($w = L\psi + s$). Ultimately, the detector will measure a three-dimensional data set where one dimension denotes the time and the other two denote the pixel coordinates of the detector, and each pixel sees intensity modulations in the time domain. With the data reduction procedure outlined by Schober *et al.* (2019) and Oda *et al.* (2020), the modulations can be shifted by a known phase over all the pixels before they are integrated spatially across the detector along h, yielding a one-dimensional intensity oscillation in the time domain, as given in equation (5). The contrast of the modulation can therefore be given by the amplitude of the one-dimensional oscillation. A higher contrast will yield a higher sensitivity to a small change in neutron energy. Therefore, the dependence of the contrast as a function of the scattering angle yields the resolution function of the MIEZE setup. To calculate the resolution function, the detector thickness is assumed to be zero:

$$I(2\theta, t) = \int_{-H}^{H}\int_{-S}^{S}\int_{-W}^{W} \cos\left[\Phi(2\theta, \omega_1, B_1, w, s, h, t)\right] \mathrm{d}w\, \mathrm{d}s\, \mathrm{d}h. \quad (5)$$

3.1. The phase aberrations of a regular MIEZE

First, to demonstrate the phase aberration problem of a conventional MIEZE, calculations have been performed by setting the field in the MWPs to zero in equation (1). In the calculation, the parameters are chosen such that $L = 5$ m, $L_1 = 4$ m, $L_2 = 2$ m, $L_s = 2$ m, $2H = 100$ mm and $\delta = 30$ mm, which are very close to the parameters of the existing RESEDA instrument at FRM-II (Franz *et al.*, 2019) and the VIN ROSE instrument at J-PARC (Hino *et al.*, 2013). For demonstration purposes, a parallel beam is used for this calculation. The contrast of the intensity modulation has been plotted in Fig. 2 as a function of scattering angle (2θ) for various frequencies (Δf) and sample sizes ($2S$). The peak contrast of the resolution function is always centered at zero scattering angle and the contrast of the modulation decreases rapidly as scattering angle increases, especially for large sample size ($2S$) and high RF frequency differences (Δf). For example, for $\Delta f = 100$ kHz and $2S = 10$ mm, it is impossible to measure the scattering at a scattering angle of 20° with a vanishing contrast.

To understand the results intuitively, I have calculated the modulations observed on the detector at a scattering angle of $2\theta = 20^\circ$. Note that the calculations performed in the following sections take a realistic beam with the divergence angle

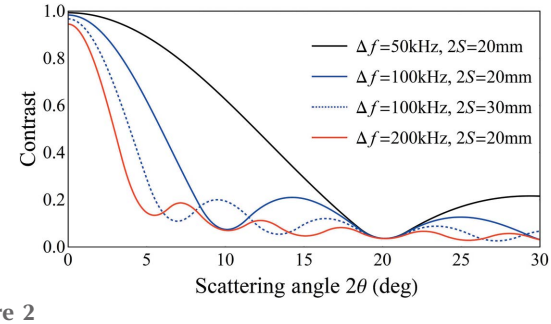

Figure 2
The contrast of the modulation as a function of the scattering angle 2θ when changing the frequency difference between the two RF flippers (Δf) and the size of the sample ($2S$). The two RF flippers are maintained in time focusing.

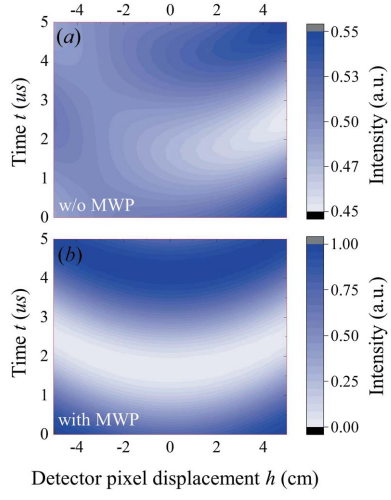

Figure 3
The intensity modulations observed on the detector along the transverse direction (*a*) with no MWPs, (*b*) with MWPs at a scattering angle of $2\theta = 20^\circ$. In this calculation, $\lambda = 5.5$ Å, $\Delta f = 100$ kHz, $2S = 20$ mm, $L = 5$ m and $2W = 40$ mm.

defined as $\psi = (w - s)/L$. As shown in Fig. 3, without the correction provided by the MWPs, the contrast of the modulations in the time domain is low across all the pixels of the detector. Setting the magnetic fields inside the MWPs according to equation (4) allows the contrast of the modulations to be fully recovered on each pixel. Along the transverse direction of the detector, the phase of the modulation is monotonically shifted towards the edges of the detector due to the monotonic increase in the neutron TOF. Because of the 'coherent' scattered beam prepared by the MWPs, the phase variation measured by the detector can be corrected by post data reduction as outlined by Schober *et al.* (2019) and Oda *et al.* (2020), which is applied in all the following calculations.

3.2. The scattering angle and frequency dependence of the phase correction

The resolution function of the MIEZE setup with the MWPs has been calculated and plotted in Fig. 4 by scanning the scattering angle and the difference of the magnetic field between the two MWPs, where the time focusing and space focusing are maintained for the RF flippers and MWPs, respectively. As one can see, for any given scattering angle, the contrast of the modulation can be maximized by adjusting the difference of the magnetic fields inside the two MWPs (ΔB). Namely, the resolution function of the MIEZE setup can be optimized by the MWPs such that the highest sensitivity can be fully recovered at any scattering angle of interest. This would allow the MIEZE instrument to reach any scattering angle without compromising the contrast of the intensity modulation or the size of the sample. It also shows that the steering condition obtained for the MWPs from the first-order approximation [equation (4)] agrees well with the optimum field calculated from equation (1). As the frequency of the modulation increases, the window of solid angle with high-contrast modulations gets narrower. Therefore, for a given detector occupying a finite solid angle, it is critical to apply the post data reduction procedure, especially for high-frequency oscillations. While the contrast of the modulation is high at low scattering angles, as shown in Fig. 4(*c*), it will further increase as the scattering angle increases. As shown in Fig. 1(*c*), this could be explained by the diminishing effective sample size and thus increasing coherence as the scattering angle approaches $2\theta = 90°$, which has been discussed in the previous sections.

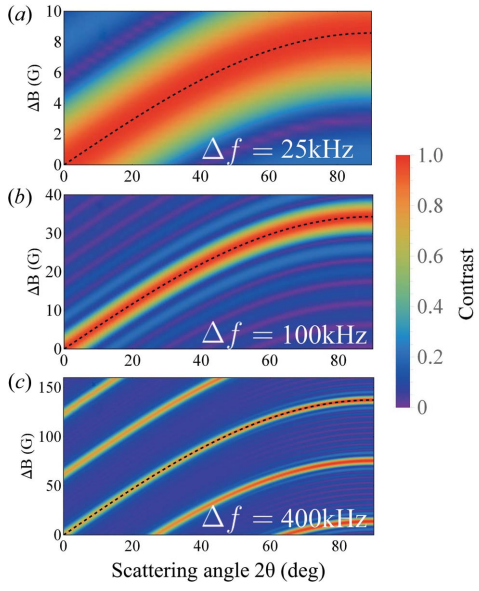

Figure 4
The contrast of the modulation as a function of the scattering angle (2θ) and the difference of the magnetic fields between the MWPs ($\Delta B = B_2 - B_1$) for three different frequencies: (*a*) Δf = 25 kHz, (*b*) Δf = 100 kHz and (*c*) Δf = 400 kHz. The dashed black lines denote the optimum setting of the two MWPs directly obtained from the steering condition given in equation (4), which show great agreement. In this calculation, λ = 5.5 Å, $2S$ = 20 mm, L = 5 m, $2W$ = 40 mm and $2H$ = 100 mm, which corresponds to a divergence of 0.34° in full width at half-maximum (FWHM) for the incoming beam.

3.3. Wavelength dependence of the phase correction

It has been shown by equation (4) that the optimum fields of the MWPs are wavelength independent. The applicability of this method at different neutron wavelengths is now calculated, where a continuous spectrum of neutrons is scanned simultaneously. The calculations are performed with two RF frequencies (Δf = 200, 400 kHz). The scattering angle is fixed to be 2θ = 20°. For each setting, the fields of the MWPs are optimized and the neutron wavelength is swept to obtain the resolution function. For comparison, the resolution function of conventional MIEZE in direct transmission geometry has also been calculated and included in Fig. 5. With the correction, the contrast of the modulations at the 20° scattering angle can be fully recovered as in the direct transmission geometry. As the modulation frequency and wavelength increase, the total Larmor phase of neutron spin, as well as its phase aberration, gets higher. Therefore, the peak contrast will slightly drop towards longer wavelength and higher frequency. The ability to maintain a high contrast on a wide-bandwidth neutron spectrum means the correction method proposed here is

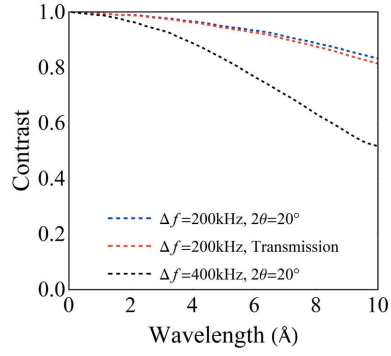

Figure 5
The variation of the peak value of the resolution function as a function of wavelength for various frequencies. For each case, the field in the MWP has been optimized according to equation (4). The parameters for the calculation are $2W$ = 40 mm, $2H$ = 10 mm and $2S$ = 20 mm. For comparison, the calculation of MIEZE in transmission geometry has also been included.

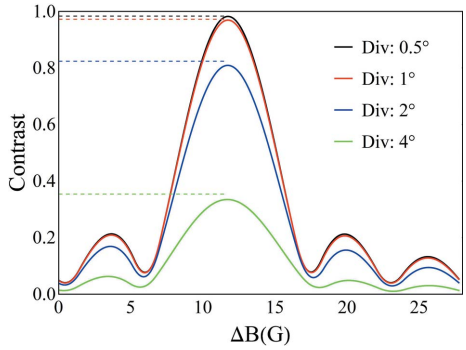

Figure 6
The variation of the resolution function as a function of field difference between the two MWPs (ΔB) for various beam divergences. The parameters for the calculation are $2\theta = 20°$, $\Delta f = 100$ kHz and $2S = 20$ mm. The dashed lines indicate the polarization of the conventional MIEZE setup in direct transmission with no MWPs, where a sample with the same effective size has been used as in the scattering beam [$2S' = 2S\cos(20°)$]. The beam divergence angle is given in FWHM.

suitable for accepting a broad wavelength band at both pulsed and continuous neutron sources.

3.4. Divergence dependence of the phase correction

According to equation (3), the magnetic field required for the MWPs is independent of the beam divergence to the first order. In this part, I will calculate and investigate the divergence dependence of the correction efficiency. As shown in Fig. 6, when the beam divergence increases, the contrast of the modulations will decrease slightly below 2° but dramatically above 2°. To determine the origin of such an effect, I have also calculated the contrast of the conventional MIEZE setup without the MWPs in the transmission direction using a sample with the same effective size [$2S' = 2S\cos(20°)$], the results of which are denoted by the dashed horizontal lines in Fig. 6. With the correction provided by the MWPs, the peak contrast of the MIEZE setup at a scattering angle of 20° is the same as for the direct geometry MIEZE for a sample with the same effective size. Basically, a higher beam divergence will introduce a larger variation of a neutron's TOF prior to its interaction with the sample even in the direct transmission geometry, where no phase correction is required. In a scattering geometry, the introduction of the MWPs would correct the phase aberration such that the same contrast as in the transmission geometry can be fully recovered with no additional divergence dependence.

4. Discussion and conclusions

Using two magnetic Wollaston prisms, I have presented an approach to correct for the first-order Larmor phase aberration of MIEZE caused by the transverse size of the sample. With this approach, the resolution function of MIEZE can be modified such that the contrast of the intensity modulation can be maximized at any scattering angle of interest. In contrast to the approach of rotating the RF flippers (Dadisman *et al.*, 2022), the approach with MWPs can shape the wavefront at the sample position precisely such that the correction efficiency is independent of the beam divergence and neutron wavelength. Such a correction approach with MWPs will be demonstrated in a future experiment. Though this approach allows MIEZE to work at a wide scattering angle, MIEZE is still limited to use at a finite solid angle. As discussed by Weber *et al.* (2013), Brandl *et al.* (2011) and Martin (2018), the geometry of the sample would affect the resolution function of MIEZE and thus the contrast of the modulations. Unfortunately, such limitation still exists for the method proposed here unless one can shape the wavefront to any arbitrary shape to match the geometry of the sample. As the thickness of the sample increases, higher phase aberrations would be expected due to the larger variation of the TOF from the sample to the detector, regardless of the phase correction mechanism provided by the MWPs. To achieve the best efficiency of correction and thus contrast, a flat and thin sample is always preferred for this method.

While the calculation is based on a conventional MIEZE instrument with no additional neutron optics in between the RF flippers, for some MIEZE instruments, special optics are embedded in between the two RF flippers to either increase the neutron flux or minimize the phase aberrations; the performance of the correction methodology proposed here would need to be reevaluated according to the specific design of the instrument. Currently, only transverse magnetic Wollaston prisms have been developed (Li *et al.*, 2014; Pynn *et al.*, 2009), which means it would be easier to correct for the phase aberration of MIEZE in the transverse configuration, such as at the VIN ROSE instrument at J-PARC. Although one could adiabatically change a longitudinal magnetic field to the transverse direction such that the transverse MWP can also be used for longitudinal MIEZE like at the RESEDA instrument, the magnetic fields would need to be carefully designed and simulated to ensure the uniformity of magnetic field integral across the beam. Therefore, for longitudinal MIEZE, the approach of rotating the RF flippers might be preferable. With the magnetic fields in the MWP well confined, the MWPs can be easily coupled to other spin manipulation components, such as the RF flippers or guide fields. If both the MWPs and RF flippers are superconducting (Dadisman *et al.*, 2020), they can share the same vacuum chamber and cryogenics, which means the whole setup would be very compact. With the RF flippers and MWPs combined, in a quantum picture, the two neutron spin states can be separated in both time and space domains. Such a setup could also be potentially used for a space–time interferometer to measure the mesoscopic space and time correlation function $G(r, t)$ (Van Hove, 1954).

Acknowledgements

I would like to express my gratitude and appreciation to Steven Parnell (Delft University of Technology), Roger Pynn, Steve Kuhn (Indiana University Bloomington) and Georg Ehlers (Oak Ridge National Laboratory) for proofreading the manuscript.

Funding information

This work was sponsored by the Laboratory Directed Research and Development Program of Oak Ridge National Laboratory, managed by UT-Battelle, LLC, for the US Department of Energy. This material is based upon work supported by the US Department of Energy, Office of Science, Office of Basic Energy Sciences under contract No. DE-AC05-00OR22725.

References

Blackburn, E., Hiess, A., Bernhoeft, N., Rheinstädter, M. C., Häußler, W. & Lander, G. H. (2006). *Phys. Rev. Lett.* **97**, 057002.

Brandl, G., Georgii, R., Häußler, W., Mühlbauer, S. & Böni, P. (2011). *Nucl. Instrum. Methods Phys. Res. A*, **654**, 394–398.

Brandl, G., Lal, J., Carpenter, J., Crow, L., Robertson, L., Georgii, R., Böni, P. & Bleuel, M. (2012). *Nucl. Instrum. Methods Phys. Res. A*, **667**, 1–4.

Dadisman, R., Ehlers, G. & Li, F. (2022). *Rev. Sci. Instrum.* **93**, 013301.

Dadisman, R., Wasilko, D., Kaiser, H., Kuhn, S. J., Buck, Z., Schaeperkoetter, J., Crow, L., Riedel, R., Robertson, L., Jiang, C., Wang, T., Silva, N., Kang, Y., Lee, S.-W., Hong, K. & Li, F. (2020). *Rev. Sci. Instrum.* **91**, 015117.

Farago, B. & Mezei, F. (1986). *Phys. B + C*, **136**, 100–102.

Franz, C., Säubert, S., Wendl, A., Haslbeck, F. X., Soltwedel, O., Jochum, J. K., Spitz, L., Kindervater, J., Bauer, A., Böni, P. & Pfleiderer, C. (2019). *J. Phys. Soc. Jpn*, **88**, 081002.

Gähler, R., Golub, R. & Keller, T. (1992). *Physica B*, **180–181**, 899–902.

Geerits, N., Parnell, S. R., Thijs, M. A., van Well, A. A., Franz, C., Washington, A. L., Raspino, D., Dalgliesh, R. M. & Plomp, J. (2019). *Rev. Sci. Instrum.* **90**, 125101.

Godfrin, P. D., Hudson, S. D., Hong, K., Porcar, L., Falus, P., Wagner, N. J. & Liu, Y. (2015). *Phys. Rev. Lett.* **115**, 228302.

Golub, R. & Gähler, R. (1987). *Phys. Lett. A*, **123**, 43–48.

Golub, R., Gähler, R. & Keller, T. (1994). *Am. J. Phys.* **62**, 779–788.

Hank, P., Besenböck, W., Gähler, R. & Köppe, M. (1997). *Physica B*, **234–236**, 1130–1132.

Haslbeck, F., Säubert, S., Seifert, M., Franz, C., Schulz, M., Heinemann, A., Keller, T., Das, P., Thompson, J. D., Bauer, E. D., Pfleiderer, C. & Janoschek, M. (2019). *Phys. Rev. B*, **99**, 014429.

Hino, M., Oda, T., Kitaguchi, M., Yamada, N. L., Sagehashi, H., Kawabata, Y. & Seto, H. (2013). *Phys. Proc.* **42**, 136–141.

Keller, T., Aynajian, P., Habicht, K., Boeri, L., Bose, S. K. & Keimer, B. (2006). *Phys. Rev. Lett.* **96**, 225501.

Kindervater, J., Stasinopoulos, I., Bauer, A., Haslbeck, F. X., Rucker, F., Chacon, A., Mühlbauer, S., Franz, C., Garst, M., Grundler, D. & Pfleiderer, C. (2019). *Phys. Rev. X*, **9**, 041059.

Li, F., Parnell, S. R., Bai, H., Yang, W., Hamilton, W. A., Maranville, B. B., Ashkar, R., Baxter, D. V., Cremer, J. T. & Pynn, R. (2016). *J. Appl. Cryst.* **49**, 55–63.

Li, F., Parnell, S. R., Hamilton, W. A., Maranville, B. B., Wang, T., Semerad, R., Baxter, D. V., Cremer, J. T. & Pynn, R. (2014). *Rev. Sci. Instrum.* **85**, 053303.

Li, F. & Pynn, R. (2014). *J. Appl. Cryst.* **47**, 1849–1854.

Liu, B., Wang, Z., Wang, Y., Huang, C. & Sun, G. (2020). *J. Instrum.* **15**, P04007.

Martin, N. (2018). *Nucl. Instrum. Methods Phys. Res. A*, **882**, 11–16.

Mezei, F. (1972). *Z. Phys.* **255**, 146–160.

Mezei, F., Pappas, C. & Gutberlet, T. (2003). *Neutron Spin Echo Spectroscopy: Basics, Trends and Applications*, Lecture Notes in Physics 601, 1st ed. Berlin, Heidelberg: Springer.

Murani, A. P. & Mezei, F. (1980). *Neutron Spin Echo*, pp. 104–112. Berlin, Heidelberg: Springer.

Oda, T., Hino, M., Endo, H., Seto, H. & Kawabata, Y. (2020). *Phys. Rev. Appl.* **14**, 054032.

Pynn, R., Fitzsimmons, M., Lee, W., Stonaha, P., Shah, V. R., Washington, A., Kirby, B., Majkrzak, C. & Maranville, B. (2009). *Physica B*, **404**, 2582–2584.

Rheinstädter, M. C., Häußler, W. & Salditt, T. (2006). *Phys. Rev. Lett.* **97**, 048103.

Säubert, S., Kindervater, J., Haslbeck, F., Franz, C., Skoulatos, M. & Böni, P. (2019). *Phys. Rev. B*, **99**, 184423.

Schober, A., Wendl, A., Haslbeck, F. X., Jochum, J. K., Spitz, L. & Franz, C. (2019). *J. Phys. Commun.* **3**, 103001.

Van Hove, L. (1954). *Phys. Rev.* **95**, 249–262.

Weber, T., Brandl, G. R., Georgii, R., Häußler, W., Weichselbaumer, S. & Böni, P. (2013). *Nucl. Instrum. Methods Phys. Res. A*, **713**, 71–75.

Zhao, J., Hamilton, W. A., Lee, S.-W., Robertson, J. L., Crow, L. & Kang, Y. W. (2015). *Appl. Phys. Lett.* **107**, 113508.